



Heat generation, plastic deformation and residual stresses in friction stir welding of aluminium alloy

Omar S. Salih^{a,b,*}, Hengan Ou^{a,*}, Wei Sun^a

^a Department of Mechanical, Materials and Manufacturing Engineering, University of Nottingham, University Park, Nottingham NG7 2RD, UK

^b Department of Applied Mechanical Engineering, Engineering Technical College-Baghdad, Middle Technical University, Baghdad, Iraq

ARTICLE INFO

Keywords:

Friction stir welding
Coupled Eulerian-Lagrangian
Thermal history
Residual stress
Neutron diffraction
Weld quality

ABSTRACT

The interactions among thermal history, plastic deformation and residual stresses in the friction stir welding (FSW) process under different welding parameters have been widely considered a crucial issue and still not fully understood. In the present study, a novel three-dimensional fully coupled thermo-mechanical finite element (FE) model based on Coupled Eulerian-Lagrangian approach (CEL) has been developed to simulate the FSW process of aluminium alloy AA 6082-T6 and to analyse the thermo-mechanical interaction mechanisms under different welding conditions. The numerical model successfully simulates the plunge, dwell, and welding steps in FSW and captures the evolution of temperature, plastic deformation, and residual stresses in the welded joint. The obtained results were validated by experimental testing with observed cross-weld thermal history, optical macrography and residual stress measurement using the neutron diffraction technique. The results reveal that the tool rotation speed governs the temperature evolution; the peak temperature increased from 740 to 850 °K when the tool rotation speed rose from 800 to 1100 rpm. The rotational speed also affected the plastic deformation, material flow, and the volume of material being stirred during the welding process. Higher plastic deformation is formed in the stirring zone by increasing the tool angular velocity. This behaviour led to an increase in the stirring effect of the welding tool, reduction of the tunnel defect size and enhancing the quality of weldments. The distribution of residual stresses in different zones of the FSW joints has been found to have an M-shaped profile. A significant tensile residual stress is characterised in the edge of the nugget zone in both longitudinal and transverse directions, balanced by compressive stresses in the thermo-mechanically affected zone, heat-affected zone and base metal. The presented FE modelling provides a reliable insight into the effects of the welding parameters on the weld quality of FSW joints and process optimisation with minimised experimental trials.

1. Introduction

As a solid-state welding technology, friction stir welding (FSW) is a most commonly used welding technology by industry in recent years to weld aluminium, magnesium, copper and steel alloys. This joining technique is characterized by the formation of welding joints at temperatures below the melting point of base metals, which leads to an inherent advantage in improved weldability over fusion welding processes [1–3]. During FSW, heat is generated due to frictional interaction and plastic deformation under variable strain rates and complex loading conditions in the workpieces [4–6]. The desired weld quality of FSW joints in terms of achievable strength and joint soundness are strongly

affected by changing welding parameters for a controlled amount of induced heat, material flow and residual stresses [7]. In-depth knowledge of the FSW mechanisms that govern these variables is essential for the reliable prediction of weld quality. However, it is difficult to physically obtain all detailed information into the joint during the actual FSW processing due to its complexity [8,9].

To overcome this limitation, finite element (FE) methods with sufficient predictive capabilities can be used as efficient tools to reduce the required initial experimental trials for achieving optimised welding parameters [10,11]. However, the FE simulation of a multi-physical problem such as FSW involves severe plastic deformation, heat flow under varying strain rates, complex material flow, and friction

* Corresponding authors at: Department of Mechanical, Materials and Manufacturing Engineering, University of Nottingham, University Park, Nottingham NG7 2RD, UK.

E-mail addresses: omar.al-jumaili@nottingham.ac.uk, omar.s.salih@outlook.com (O.S. Salih), h.ou@nottingham.ac.uk (H. Ou).

<https://doi.org/10.1016/j.ijmecsci.2022.107827>

Received 21 February 2022; Received in revised form 6 October 2022; Accepted 7 October 2022

Available online 8 October 2022

0020-7403/© 2022 The Authors. Published by Elsevier Ltd. This is an open access article under the CC BY license (<http://creativecommons.org/licenses/by/4.0/>).

conditions is highly challenging as it needs to take into account all the phenomena of the highly nonlinear and coupled thermomechanical process [12,13]. Considerable progress has been made in the simulation of FSW processes using different modelling approaches such as computational fluid dynamics (CFD), Arbitrary Lagrangian-Eulerian (ALE) and Coupled Eulerian-Lagrangian (CEL) in recent years.

In the CFD-based model, the workpieces are often modelled as non-Newtonian fluid, and the thermo-mechanical material behaviour is analysed using viscous fluids energy, momentum and mass conservation equations [14]. Seidel and Reynolds [15] developed a two-dimensional (2D) thermal model based on fluid mechanics to investigate material flow in FSW joints. The welding process was simulated as a steady-state, laminar flow of a non-Newtonian fluid past a rotating circular cylinder (assumed the FSW tool consist of pin only). They observed that the material flow was not symmetric about the welding centreline with significant vertical mixing during FSW. However, the authors addressed a mismatch between the experimental and model results, owing to the absence of the tool shoulder, which significantly affects the mixing process. Colegrove and Shercliff [16–18] systematically investigated the material flow behaviour using different tool geometries in 2D and three-dimensional (3D) analysis. They demonstrated a novel modelling technique with slip boundary conditions. The slip model showed a significant difference in material flow when using various tool shapes, which was not apparent with the conventional stick model. Zhang et al. [19] established a 3D CFD model to quantitatively analyse the frictional and plastic deformation heat flux spatial distribution during FSW. An advanced interfacial friction model was used to capture the complex interplay between the contact states at the welding tool/workpiece interface and heat flux spatial distribution. They found that both sticking and sliding conditions happened simultaneously at different parts of the welding tool/workpiece interface. These complex conditions significantly influence the mode of heat generation and distribution. Hasan [20] used the coupled thermo-flow model (single-phase flow) and volume of fluid method (two-phase flow) techniques to predict the temperature and surface flash formation phenomena, respectively. The study showed a good agreement for temperature prediction and pointed out that using the volume of fluid model predicted the surface formation more realistically. Zhai et al. [21] developed a CFD-based numerical simulation to investigate the effect of tool tilt angle on the behaviour of heat generation and material flow in FSW. The study revealed that by increasing the tool tilt angle from 0° to 2.5°, higher heat was generated in the workpiece, which allowed the tool shoulder to retain the flow of plasticized material into the nugget zone and to reduce flash formation. Shi et al. [22,23] compared the thermal cycles and plastic material flow behaviours with and without applications of ultrasonic vibration during FSW using an integrated 3D CFD model that combined a thermo-fluid model, a computational ultrasonic field model and a welding loads model. The model results showed that the superimposing ultrasonic vibration in FSW had a minor effect on the temperature history, whilst it enhanced plastic material flow near the tool, increased welding speed and efficiency, and improved weld quality. The predicted results were in good agreement with the experimentally measured ones. Zhao et al. [24] developed a fully coupled model to analyse the effect of ultrasonic energy on the mechanisms of FSW. It was found that the ultrasound had dual effects on the contact interfacial stress state at the tool/workpiece. Firstly, ultrasonically induced friction reduction (antifriction) by changing the ratio of sliding/sticking. Secondly, the acoustic softening effect promoted dislocation movement and reduced the resistance to plastic deformation. The analysed works proved the ability of the CFD approach to simulate FSW. However, the main drawbacks of CFD based simulations were their inability to include material hardening and material's elasticity as only rigid-viscoplastic material behaviour was considered [25].

Another approach used to simulate FSW is based on Arbitrary Lagrangian-Eulerian (ALE) formulation with the adaptive re-meshing technique. In this technique, the computational mesh moves

arbitrarily in the ALE domain, and the elements optimize their shape, allowing improved handling of significant deformation, which could cause excessive mesh distortion during the simulation [26]. Thus, the ALE-based FSW simulation can be achieved within a realistic computation time and is better equipped to overcome highly distorted elements during FSW for possible convergence problems, loss of accuracy and prolonged computation time [27]. Schmidt and Hattel [28] developed a fully localised coupled thermomechanical 3D FE model using adaptive boundary conditions with the Johnson-Cook-based flow stress model to determine void-free weld conditions. The contact forces between tool and plate surfaces were defined based on Coulomb's law of friction. Their investigation showed that the defect formation in the welded joints was highly controlled by the cooling rate. Faulty material deposition behind the tool pin was achieved with a higher cooling rate. Deng and Xu [29] developed a 2D FE model using ABAQUS dynamic explicit to simulate the material flow pattern around the tool pin. The experimentally measured temperatures were applied as body loads, and plane strain conditions were assumed in the model. Constant rate slip and modified Coulomb's frictional models were used as contact interaction models between the tool pin and workpiece. Comparing both contact models showed little difference in the simulation of material flow and post-weld marker positions. However, the authors stressed that several simplifications were made in carrying out their study due to computational constraints and a lack of experimental data. Zhang et al. [30,31] extended the study to evaluate material flow and residual stresses of AA 6061-T6 FSW joints under different welding parameters in 2D and 3D modelling. Tracer particles were used to investigate the pattern of material flow during FSW. Their results showed a difference in the material flow on the advancing side (AS) and retreating side (RS), and the longitudinal residual stress increased when the traverse speed increased. Zhang [32] carried out a comparison between classical and modified Coulomb's contact models and studied their effect on the thermo-mechanical interaction process in FSW. The results showed that both contact models predicted similar results at lower angular velocity. However, when using classical Coulomb friction law at higher tool rotational speeds, the simulation failed to complete as a result of increasing the dynamic effect of the welding tool. Dialami et al. [33–35] systematically studied the material flow behaviour and defect formation during FSW using a 3D ALE model. An enhanced friction model (modified Norton's friction law) was developed to give a more accurate thermo-mechanical response by considering the effect of the non-uniform distribution of pressure under the shoulder. They demonstrated that the welding parameters strongly affected defect formation in FSW joints. By comparing both numerically and experimentally results, the proposed friction model resulted in an improved prediction capability. Andrade et al. [36,37] extended the study to determine the evolution of strain rates, torque and welding temperatures under different welding conditions and tool dimensions during FSW of aluminium alloys. The tool rotational speed and sizes were found to be the main factor governing the torque and temperature. According to the authors, the numerical model predicted strain-rate gradients and heat generation in the stirred volume with satisfactory accuracy. The above studies proved the capability of the ALE approach to model FSW. However, choosing the relative movement between the welded material and mesh to reduce the distortion of mesh was the main drawback of the ALE approach [38].

Recently, a Coupled Eulerian-Lagrangian (CEL) approach was developed and implemented in the FE code ABAQUS to deal with large deformations problems. This approach is based on an explicit time integration formulation, and it depends on Benson's contact mixture theory by tracking and computing the interface between the Eulerian domain (in this work welded material) and the Lagrangian body (in this work FSW tool) automatically [39]. Thus, this method was used to simulate applications involving large deformation and complex tool geometries because there was no need for fitting Eulerian mesh boundaries to the tool geometry [38]. Based on the CEL approach,

6 and 1 μm diamond paste. To highlight the FSW zones of weldment, acid etching was carried out with Poulton’s reagent and then investigated by Nikon optical microscope.

2.2. Residual stress measurements

Residual stress measurements were performed by neutron diffraction using the beamline ENGIN-X facility at the ISIS neutron source at Rutherford Appleton Laboratory, Oxford, UK. As can be seen in Fig. 2(a), a pulsed neutron beam with a wide energy range travelling to the sample and is scattered into two banks of detectors, each centred at a fixed angle (Bragg angle (2θ) of ± 90° to the incident beam) that allows a full diffraction pattern to be measured. When Bragg’s Law is satisfied for a lattice spacing d_{hkl} , diffraction peaks occur and are measured at times t_{hkl} elapsed after the initial pulse [46]. The concept of measuring the residual stresses by neutron diffraction is based on using lattice spacing as a strain gauge to measure the macroscopic elastic strain, which is defined by the time-of-flight (TOF) neutron strain scanner at definite locations in the bulk of the sample. Under compressive or tensile stress, the lattice spacing, d_{hkl} , for lattice planes, hkl , changing by contracts or expanding in individual grains. This change in the lattice spacing is

detected as a shift, $\theta\Delta_{hkl}$, in the hkl diffraction peak at a constant wavelength. The strain in the specific plane, ϵ_i , is calculated based on Bragg’s law, as given by Eq. (1).

$$\epsilon_i = \frac{d_{hkl}^i - d_{hkl}^0}{d_{hkl}^0} \tag{1}$$

Where d_{hkl}^i is the lattice parameter for each measurement point along with three mutually orthogonal directions, and d_{hkl}^0 is the measured strain-free inter-planar spacing. The lattice spacing measurement was done twice. Firstly, it was done in the mid-length of welded plates to measure the change in lattice spacing from the welding process (d_{hkl}^i). After that, a 4 mm thick slice of cross-weld was extracted from the same joint and location using EDM to release the strain and measure the strain-free lattice spacing (d_{hkl}^0). Both measurements were used in Eq. (1) to calculate the microstrain along the three principal directions: the normal direction (ND) perpendicular to the top surface of the plate, the longitudinal direction (LD) parallel to the weld, and the transverse direction (TD) perpendicular to the weld. Due to the ENGIN-X configuration, with a single scan, the strain is measured in two directions simultaneously; normal and longitudinal or transverse direction, based on the position of the sample. Therefore, to measure both longitudinal

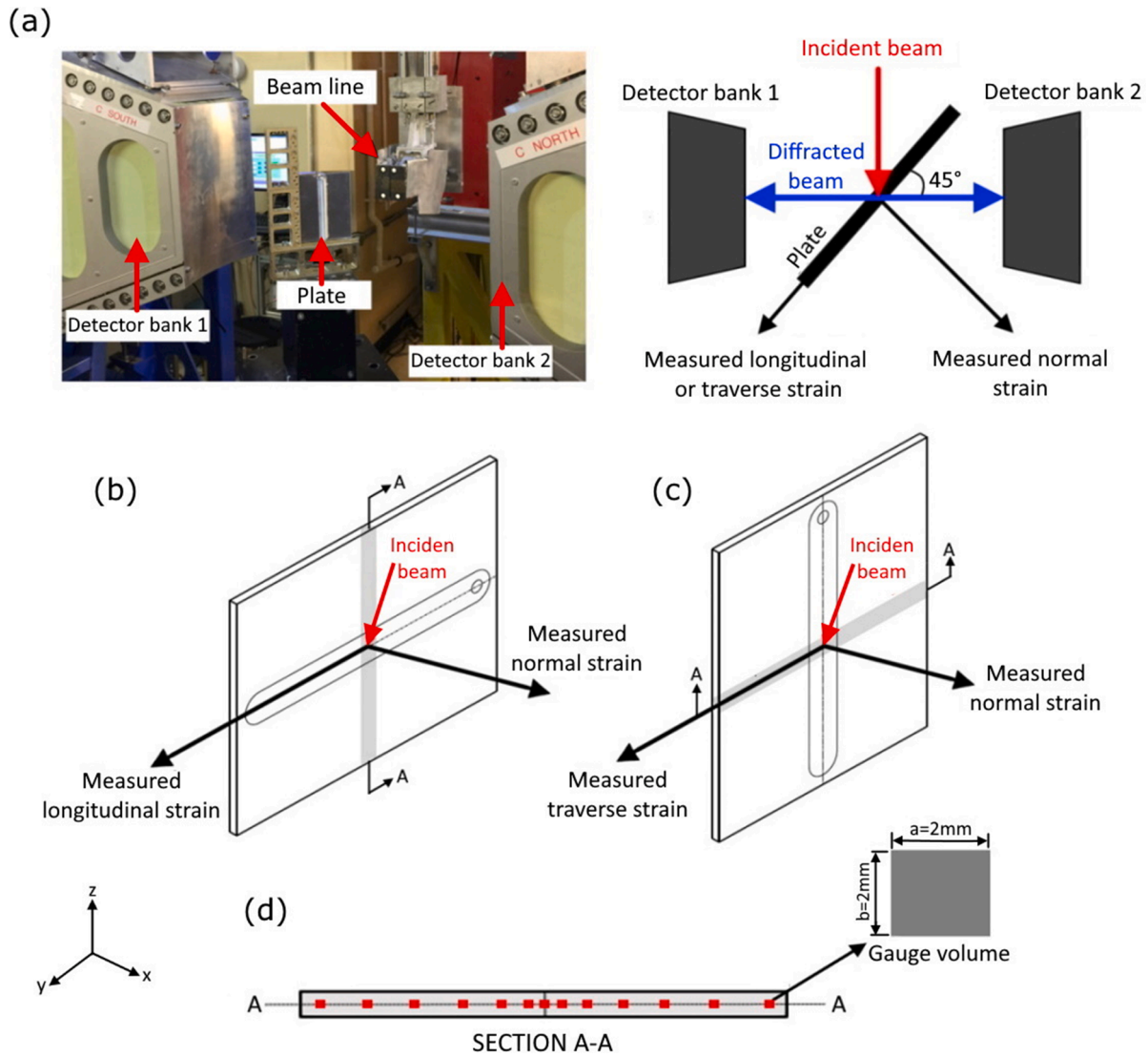


Fig. 2. Residual stress measurements by neutron diffraction. (a) A picture and schematic top view of sample position on the ENGIN-X beamline and measurement principle, (b) A schematic of the sample position to measure longitudinal strain along the grey shaded area, (c) A schematic of the sample position to measure transverse strain along the grey shaded area, and (d) Cross section showing the positions of measurement points (red squares) and gauge volume.

and transverse strains, the scan was repeated twice by changing the weld line direction (repositioning the sample). When the weld is horizontal and the angle between the plate surface plane and the incident beam is 45° , one of the two vectors was in the direction of the longitudinal strain (Y-Y) and the other vector in the direction of the normal strain (X-X), as shown in Fig. 2(b). On the other hand, when the weld line is vertical, this allows the measurement of the transverse and normal strains, as shown in Fig. 2(c). The locations of the measurements were taken in the mid-thickness of the plate in the middle of the joint line (grey shaded area) with a gradual increase in spatial resolution from the weld centre, as shown in Fig. 2(d). Two laboratory theodolites and a laser/CCTV system were used to align the sample accurately and monitor its motion. Once the sample position relative to the instrument was determined, the measured point locations could be determined automatically by inputting the coordinates data into an automated positioning system, which can be achieved using Strain SCANning Simulation Software (SSCANSS).

In a pulsed instrument, the intersection between the incident and diffracted beams defines the material volume contributing to the diffraction pattern (gauge volume) (see Fig. 2(d)), and it is controlled by slits and collimators. Two radial collimators, each having 40 vertical foil vanes made from gadolinium oxide coated Mylar, were used to constrain the detectors to receive neutrons from a small volume. To maximise the data acquisition rates, the gauge volume was adjusted based on the orientation of the sample. When measuring the strain in the TD, $2 \times 2 \times 10 \text{ mm}^3$ ‘matchstick’ gauge volume was used aligned with the direction of the weld. For the LD measurements, the gauge volume was $2 \times 2 \times 2 \text{ mm}^3$. The full diffraction spectrum was obtained from each measured point and analysed by the General Structure Analysis System (GSAS) program using multiple peaks fitting Pawley refinement. The triaxial residual stresses were calculated by Hooke’s law, given by the following equation.

$$\sigma_i = \frac{E}{1+\nu} \left[\varepsilon_i + \frac{\nu}{1-2\nu} (\varepsilon_x + \varepsilon_y + \varepsilon_z) \right] \quad (2)$$

Where E , ν , ε_x , ε_y and ε_z represent Young’s modulus, Poisson’s ratio, normal strain, longitudinal strain, and transverse strain, respectively.

3. Finite element simulation

The welding mechanisms that govern the welding temperatures, plastic deformation and residual stresses were studied through FE simulation of the FSW process. This section details the methodology and solution strategy used to model the FSW process, thermal and physical properties of base materials, load and boundary conditions, and meshing.

3.1. FE modelling

A 3D coupled thermo-mechanical FE model based on the Coupled Eulerian-Lagrangian (CEL) approach using an explicit algorithm has been developed in ABAQUS to simulate the whole FSW process (plunge,

dwelling and welding steps) and predict thermal history, material flow and joint soundness and residual stresses in the FSW joint. In modelling the FSW process, the tool rotation and plunging induced mesh distortion near the tool–plate interface is overcome with the CEL approach, as this approach allowed plunging of a Lagrangian rigid body inside the Eulerian media where the base metal flowed through fixed nodes. More details about the governing equations of the CEL approach are provided in the Appendix. The FSW tool was defined as a rigid isothermal Lagrangian body, while the plate was defined as an Eulerian body, as shown in Fig. 3(a). The FSW tool was simulated with shoulder and pin having dimensions and profile consistent with the experiment’s ones, as shown in Fig. 3(b), and its movement is controlled by a reference point (RP). Similarly, as in the experiment, the tool was tilted by 2° , and a plunge depth of 0.2 mm was applied during the welding step.

As noticed in the experimental work of this study, the change in the welding temperature was less pronounced after 20 mm in the lateral distance from the weld centre. Therefore, the Eulerian domain (plate) geometry was simulated as a local domain with 50 mm length and width as a trade-off between the model accuracy and computing time. The local square cuboid shape consisted of two regions, as shown in Fig. 3(a). The first region is the material region (red colour), having a thickness of 4 mm (equal to the plate thickness used in the experimental work) and assigned with the base metal (AA 6082-T6) properties. The second region is the material-free region (blue colour), having a thickness of 2 mm and left empty without material properties. In the plunge and dwell step, a constant volume approach was used, and there was no movement in the material. Meanwhile, a control volume approach was performed in the welding step. The welding speed was defined as a longitudinal velocity of inflow and outflow of material over Eulerian domain boundaries instead of the longitudinal motion of the FSW tool (Fig. 3(a)).

3.2. Material properties

The accuracy of simulation results of a multi-physics process such as FSW depends strongly on the definition of base material properties. In FSW, the welding temperature ranges from room temperature to around the solidus temperature. As it is known that the properties of metals are functions of temperature [31], the relevant mechanical and physical properties of the base metal (AA 6082-T6) were defined as temperature-dependent, and it was taken from several literature works [40,47–49] and presented in Fig. 4.

Besides the gradient in temperature, the base metal is also subjected to complex strain and strain rates during the welding process. The base metal plastic behaviour was modelled by using Johnson-Cook constitutive model. This model is an empirical viscoplastic constitutive model and a particular type of Mises plasticity model used to depict the work hardening, thermal softening and strain rate hardening of the metal. Thus, it is suitable for high strain-rate deformation and temperature, as confirmed by Al-Badour et al. [40] and Tongne et al. [38]. The von Mises flow stress σ_o , according to the Johnson-Cook constitutive model is expressed in Eq. (3).

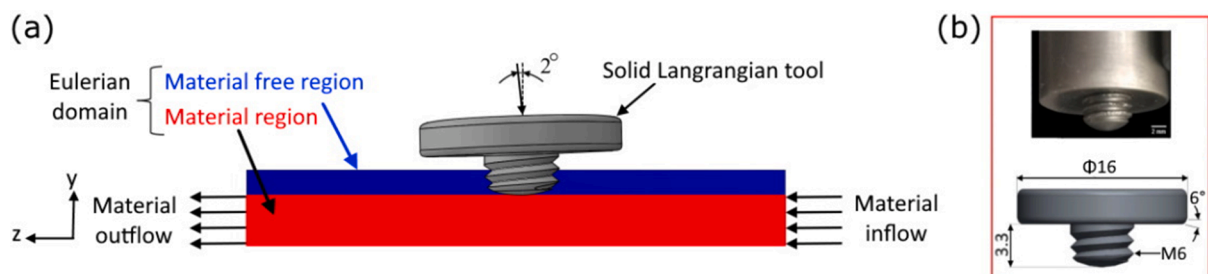


Fig. 3. Finite element implementation. (a) Problem set-up in the CEL finite element simulation for the FSW process showing the Eulerian domain (material region (red colour) and material-free region (blue colour)), tool configuration, and material inflow and outflow during the welding step, (b) Geometry detail of FSW tool used in the experiment and model. (Dimensions in mm).

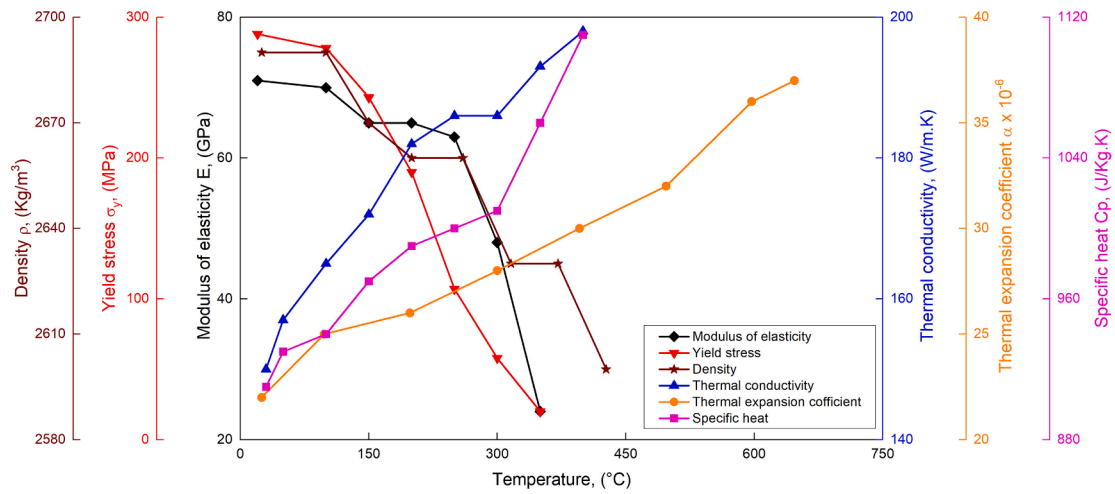


Fig. 4. Mechanical and physical properties of AA 6082 aluminium alloy as a function of temperature used in the CEL model, including density, yield stress, modulus of elasticity, thermal conductivity, thermal expansion coefficient, and specific heat [40,47–49].

$$\sigma_o = [A + B\varepsilon^n] \left[1 + C \ln \left(\frac{\dot{\varepsilon}}{\dot{\varepsilon}_o} \right) \right] \left[1 - \left(\frac{T - T_o}{T_m - T_o} \right)^m \right] \quad (3)$$

Where ε , $\dot{\varepsilon}$, $\dot{\varepsilon}_o$, T , T_o and T_m represent equivalent plastic strain, strain rate, reference strain rate, environment temperature, reference temperature, and material melting temperatures, respectively. A , B , C , n and m are material constants, where A , B and C are the initial yield strength, hardening modulus, and strain-rate dependency, respectively. The Johnson-Cook parameters used in this model were obtained from Jaspers and Dautzenberg [50] work based on the Split Hopkinson pressure bar (SHPB) test for AA 6082-T6 and defined in Table 1.

3.3. Contact interaction and boundary conditions

A critical part of the numerical modelling of the FSW process is the contact condition because the workpiece and tool have multiple contacts among themselves [51]. The general contact algorithm is used to define all incorporated contacts between the workpiece and tool. Also, the contact definition on the tool-plate interface, i.e., normal and tangential formulation, is considered part of the solution using hard contact pressure and penalty contact algorithm, respectively.

The nature of heat generation in the FSW process is thermo-mechanical, i.e. heat is generated due to frictional heat action between the workpiece and FSW tool as well as from base metal plastic deformation, as expressed in Eq. (4), and both are considered in the analysis.

$$\dot{q} = \dot{q}_f + \dot{q}_p \quad (4)$$

Where \dot{q} , \dot{q}_f and \dot{q}_p represent the rate of total heat generation, rate of frictional heat generation, and rate of heat generation due to plastic deformation, respectively.

Coulomb's friction law defines the friction at the contact interface between the Eulerian domain and the Lagrangian body, as given in Eq. (5).

$$\tau_s = \mu p \quad (5)$$

Where τ_s , μ and p are frictional shear stress, frictional coefficient, and

Table 1
Johnson-Cook constitutive parameters for AA 6082-T6 aluminium alloy [50].

A (MPa)	B (MPa)	C	n	m	T_o (°K)	T_m (°K)
428.5	327.7	0.00747	1.008	1.31	298	855

contact pressure at the tool-workpiece interface, respectively. This law predicts the mutual motion between two segments, whether they slide or stick. The sliding condition is met when the contact shear stress is smaller than the material yield shear stress, and thus heat is generated by friction, as given in Eq. (6).

$$\dot{q}_f = \phi(\tau_s \dot{\gamma}) \quad (6)$$

Where ϕ and $\dot{\gamma}$ are the frictional heat factor, and slip rate, respectively.

On the other hand, if the friction shear stress is larger than the yield shear stress of the base metal, the sticking state is fulfilled, and the heat generated by plastic deformation, as expressed in Eq. (7).

$$\dot{q}_p = \eta \sigma_{ij} : \dot{\varepsilon}_{ij} \quad (7)$$

Where η , σ_{ij} and $\dot{\varepsilon}_{ij}$ represent the Taylor-Quinney ratio that measures the fraction of plastic work converted to heat, stress tensor, and plastic strain rate, respectively.

The calculations of heat generation and material flow during FSW mainly depend on selecting the accurate value of the friction coefficient. However, Nandan et al. [52] pointed out that it is difficult to determine this value from fundamental principles or experiments relevant to the FSW conditions. Thus, different friction coefficient values ranging from 0.3 to 1.2 were used in the previous studies [53–57]. Kumar et al. [58] found that the temperature of the base material remarkably controls the friction coefficient between steel and aluminium, and it ranges from around 0.2 to 1.4 when the temperature of the base material increases from around 100 °C to 450 °C. Thus, a higher friction coefficient is used with a higher tool rotation speed. Furthermore, in the dwelling and welding stages, flow stress underneath the outer edge of the shoulder becomes more significant than the shear stress at the interface, which narrows down in the sticking zone. Thus, a higher friction coefficient on the contact surface helps obtain a larger stick-slip ratio and a much higher total heat generation rate [44]. This finding is confirmed by He et al. [12] work, as they reported that a larger void size resulted from a lower friction coefficient. Thus based on the above reasons, a high friction coefficient of 0.8 was used in the current study, as it was also confirmed by Al-Badour et al. [40] that this value gave a reasonable prediction of the size of the formed defect.

The energy balance equation controls the thermo-mechanical response, as given in Eq. (8) [59,60].

$$\rho c_p \frac{\partial T}{\partial t} = k T_{ii} + \eta \sigma_{ij} \dot{\varepsilon}_{ij} \quad (8)$$

Where ρ , c_p , k , T_{ii} and t are mass density, specific heat capacity, the

thermal conductivity of the material, Laplace differential operator on temperature, and time, respectively. It is assumed that 90% of plastic work and 100% of the frictional energy were converted to heat by defining plastic heat fraction and frictional heat factor as 0.9 and 1.0, respectively, similar to that used in other work [61–64].

The boundary conditions applied to the workpiece can significantly affect the model results. Thermal and velocity boundary conditions are applied to the domain at different stages to represent the physical situation accurately. To model the heat dissipation from the workpiece surfaces into the surrounding environment, heat radiation and convection models were defined to dissipate the heat through the boundaries, as given in Eq. (9).

$$-k \frac{\partial T}{\partial n_s} = \sigma_b \epsilon_b (T^4 - T_a^4) + h_a (T - T_a) \quad (9)$$

Where k , n_s , σ_b , ϵ_b , h_a and T_a represent thermal conductivity of the material, heat dissipation surface in normal direction, Stefan-Boltzmann constant, emissivity, convective heat transfer coefficient, and ambient temperature, respectively. More details about the thermal-stress analysis are provided in the Appendix.

Tool displacement and rotation were constrained to a reference point (RP) to control the position of the tool and to apply the rotational tool speed. The tool was assigned to 800 or 1100 rpm rotational speed for all FSW steps, as shown in Table 2. The velocity boundary conditions of the material were constrained in the bottom and sides of the Eulerian domain ($V_x = V_y = 0$) in plunging, dwelling, and welding steps to avoid the loss of material (control volume) as defined in Table 2 and shown in Fig. 5(a) and (b). Meanwhile, in the welding step, the velocity constraints at the boundaries for the welding speed were defined as inflow and outflow material velocity ($V_z = 200$ mm /min), as shown in Fig. 5 (b).

3.4. FE mesh and element type

The full mesh adopted for the workpiece and FSW tool is shown in Fig. 5(c). EC3D8RT eight-node thermally coupled linear brick, multi-material, reduced integration with hourglass control, and four degrees of freedom elements were used in the Eulerian domain (workpiece). In Eulerian analyses, the boundaries of each Eulerian material were reconstructed based on the computed volume fraction data for each Eulerian material in an element in each time increment. The material boundaries within an element were approximated as simple planar facets by the interface reconstruction algorithm. This assumption produces a simple, approximate material surface that may be discontinuous between neighbouring elements. Thus, fine mesh resolution is required to determine the material's location within an element accurately. Based on the above reason and the need to reduce computational time, the Eulerian domain was meshed using a bias meshing technique; i.e. a fine mesh was generated in the interaction zone of the tool-workpiece and a coarse mesh for the rest of the domain. The FSW tool was meshed using a three-noded rigid triangular facet element (R3D3).

Table 2
CEL model boundary conditions.

Boundary conditions	Tool rotation speed (rpm)	Weld I		Weld II	
		Plunge and dwell steps	Weld step	Plunge and dwell steps	Weld step
Vx (mm/min)	0	0	0	0	0
Vy (mm/min)	0	0	0	0	0
Vz (mm/min)	0	200	0	0	200

4. Results and discussion

Several parameters influence the weld quality of the FSW joint, and one of them is the tool rotation speed. The current research evaluated the effect of two different rotational speeds, 800 and 1100 rpm, on the thermal history, plastic deformation and material flow behaviours, and residual stresses in the FSW joint of AA 6082-T6 aluminium alloy. The predicted results of the CEL model were validated and confirmed by comparing them with the experimental results.

4.1. Analysis and validation of thermal history in FSW joints

In FSW, a certain amount of heat is required to create a local high-temperature zone in the vicinity of the welding tool to mix the welded metal, activate the dynamic recrystallization process, and form a solid-state bonding [14]. The simulated cross-weld temperature during the plunge, dwell, and welding steps for Weld I (800 rpm - 200 mm/min) and Weld II (1100 rpm - 200 mm/min) are illustrated in Figs. 6 and 7, respectively. For both welds, during the plunge step, the rotating tool pin penetrates the workpiece until the tool shoulder contacts the workpiece, and then as in the experimental work, 0.2 mm is used as shoulder plunge depth. For Weld I, it can be seen that the generated temperature in the weld centre region increases as the plunge depth increases, and it extends down from the upper to the bottom surface near the shoulder-pin junction, as shown in Fig. 6 (a-d). This can be related to the larger contact area between the FSW tool and workpiece, contributing to a large proportion of heat generation. The highest temperature occurs in the dwell step when steady-state conditions are reached, as shown in Fig. 6(e). While, in the welding step (Fig. 6(f)), there is a slight drop and stabilisation in the high temperature due to less heat concentration caused by high welding pitch (WP) (welding speed / rotational speed) (mm / rev), as it controls the exposure time at high temperature and cooling rate. For Weld II, it is clearly seen that the lowering of WP by increasing the tool rotation speed from 800 rpm to 1100 rpm led to an increase in the generated temperature with an enlargement in the high-temperature region for all welding steps, as shown in Fig. 7.

Fig. 8 shows the three-dimensional CEL simulation results of thermal distribution in Weld I and Weld II - FSW joints during the dwell and welding steps. The result proves that the region in contact with the tool shoulder is subjected to the highest thermal impact effect, where the energy density and plastic deformation are extremely high. Also, it shows that the temperature in the weld nugget area follows a 'V' shape. As explained by Nandan et al. [65], this profile resulted from the generation of more heat further away from the tool axis near the shoulder as the relative velocity between the shoulder and the workpiece increases with distance from the tool axis. In addition, it is clearly seen that the temperature profiles are non-axisymmetric for all the cases. Higher temperatures are generated in the RS than in the AS.

The predicted temperatures from the FE simulation were compared with the experimentally measured temperature by means of thermocouples during the welding process for Weld I and Weld II and presented in Figs. 9 and 10, respectively. To get the overall trend of experimental temperature distribution, each thermocouple's peak temperature was used based on its distance from the welding line, as shown in Figs. 9(b) and 10 (b). Comparisons were made along the transverse sections (cross-weld) through the tool axis in the mid-length of the joint below the top surface of the workpiece by 2 mm.

The FE model has successfully predicted the trend of temperature distribution through the weld cross-section at different monitoring locations, especially the peak temperature in the centre of the welding line. Compared with the peak temperature of the FSW joint welded at 800 rpm (Fig. 9), the maximum temperature was increased from around 740 to 850 °K when the tool rotation speed increased to 1100 rpm at a constant welding speed (Fig. 10). In addition, the temperature profile for both studied conditions shows asymmetric behaviour and becomes more significant at a higher tool rotation speed. It can be observed that a

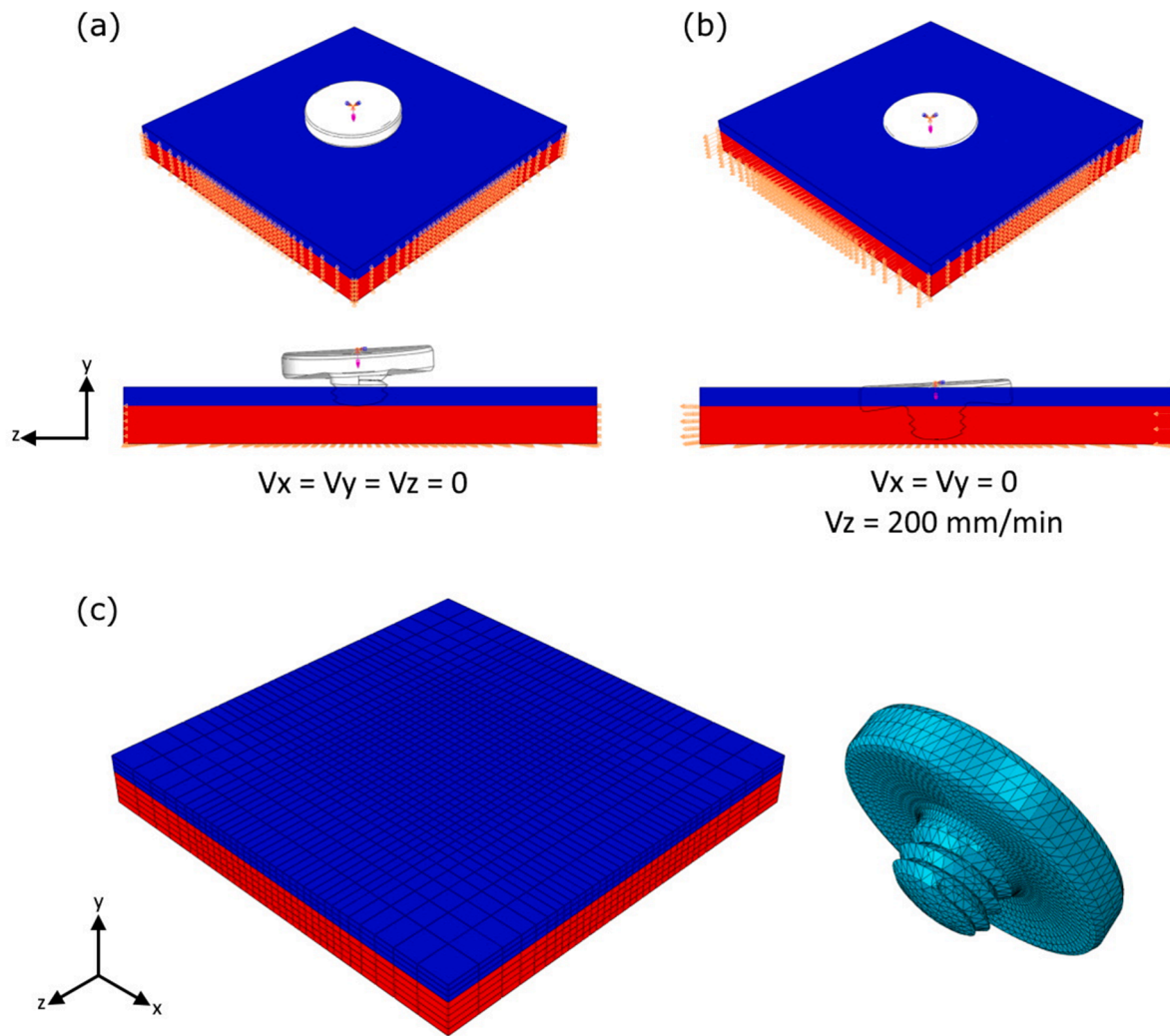


Fig. 5. Boundary conditions and mesh technique used in the CEL model. (a) Velocity boundary conditions in the workpiece during the plunge and dwell steps are equal to zero in three directions (V_x , V_y and V_z), (b) Velocity boundary conditions in the workpiece during the welding step are equal to zero in V_x and V_y direction and 200 mm/min (welding speed) in the welding direction (V_z), and (c) Mesh technique of the workpiece (bias meshing with EC3D8RT element type) and FSW tool (element type R3D3).

higher temperature was generated in the region near the tool pin toward the retreating side compared to the advancing side, which was consistent with the experimental results. Similar behaviour of thermal distribution was observed in other works [66–68]. The asymmetry behaviour of thermal distribution can be owing to one or more of the following reasons. (i) The metal flow mechanism, i.e. the FSW tool sweeps the hot softened material from the AS to the RS and additionally sweeps it into the region behind it; as the tool moves ahead, more heat is generated on the RS [66]. (ii) The design of the tool pin, Hassanamraji et al. [60] found that the generated temperature at the RS was higher than that at the AS when using the cylindrical pin. In contrast, for the conical pin, it was just the opposite. (iii) The welding parameter also affects the temperature distribution on both sides of the FSW tool. It has been reported that in the samples welded with higher travel speed, the heat generation caused by the plastic strain is higher on the RS than on the AS. It can be attributed to the asymmetrical distribution of plastic strains because the severe plastic deformation is much smaller on the AS than on the RS at a higher traverse speed [69].

The FE results indicate that the developed model can successfully predict the gradient and maximum temperature during FSW, which significantly affects the microstructural evolution and weld quality of FSW joints. However, an overestimated temperature in the region far away from the weld centreline in Weld II could be related to the larger

mesh size.

4.2. Analysis and validation of plastic deformation and joint formation

During FSW, significant plastic deformation occurs due to the interaction at the tool/workpiece interface, which controls the flow of softened welded material and forms the FSW joint. It also affects the evolution of microstructure in the weld zone by means of dynamic recrystallisation along with thermal history and influences defect formation in the welded joints. The flow of softened material around the tool is very complicated and depends on the welding parameters and tool geometry. Therefore, it is vital to study the strain distribution to understand the material flow characteristics for optimum combinations of FSW parameters, as indicated by Ke et al. [70] and Neto and Neto [71]. Fig. 11 shows the typical equivalent plastic strain (PEEQ) distribution in FSW joints during the plunge, dwell, and welding steps of Weld I. The results revealed that the equivalent plastic strain is increased as the tool plunge depth increases (Fig. 11(a–e)) and reaches the maximum during the welding step (Fig. 11(f)). In the plunge step, the maximum equivalent plastic strain happens around the tool pin. Meanwhile, it occurs on the top surface under the shoulder in the dwell and welding steps. This behaviour is also confirmed in the longitudinal weld cross-section, as shown in Fig. 11(g), and it is consistent with other

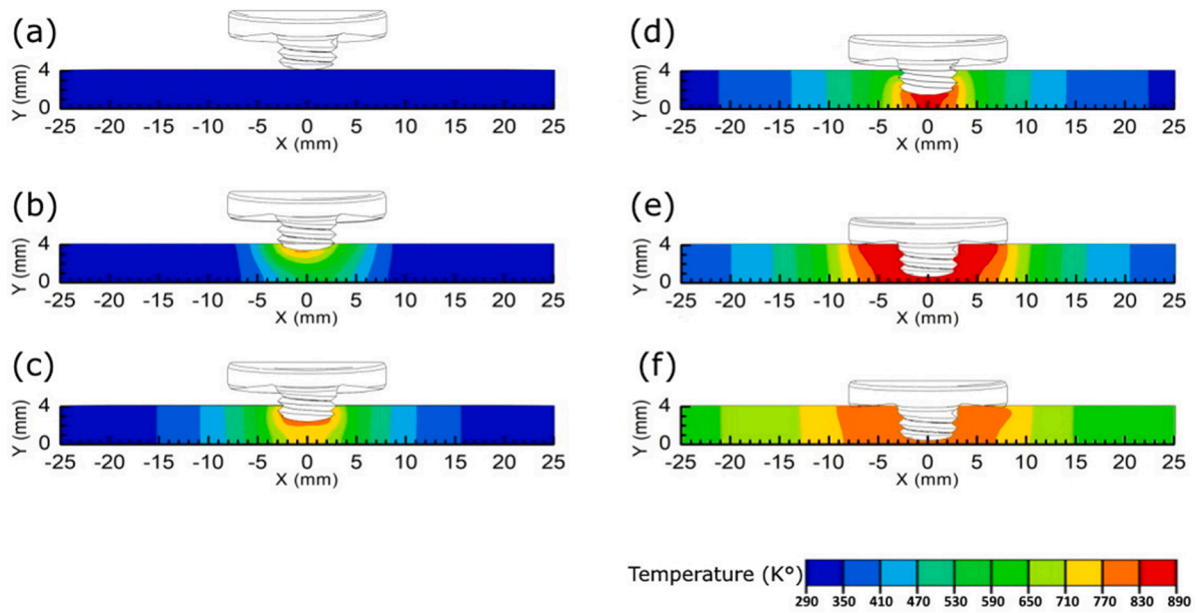


Fig. 6. Temperature field contours at the transverse cross-section of Weld I - FSW joint at different welding steps showing the increasing temperature by increasing tool plunge depth. (a-d) In the plunge step at plunge depths of 0, 0.9, 1.8 and 2.7 mm, respectively, (e) In the dwell step at a plunge depth of 3.5 mm, (f) In the welding step. (AS on the right).

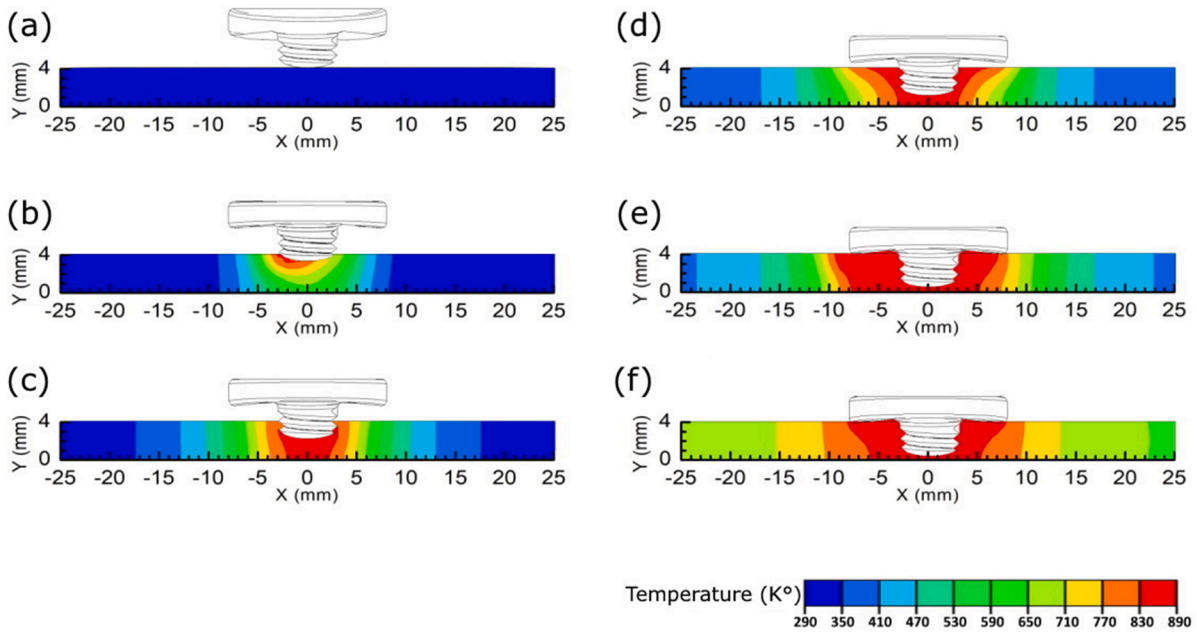


Fig. 7. Temperature field contours at the transverse cross-section of Weld II - FSW joint at different welding steps showing the increasing temperature by increasing tool plunge depth. (a-d) In the plunge step at plunge depths of 0, 0.9, 1.8 and 2.7 mm, respectively, (e) In the dwell step at a plunge depth of 3.5 mm, (f) In the welding step. (AS on the right).

studies done by Zhang and Zhang [59] and Jain et al. [72]. It can be concluded that the shoulder rotation accelerates the deformations of material near the top surface. This finding is consistent with the physical behaviour of FSW, as the maximum velocity is achieved near the shoulder edge at the top surface of the workpiece, followed by a rapid reduction away from this region [10,52].

Fig. 12 shows the predicted cross-weld equivalent plastic strain distributions for Weld I and Weld II - FSW joints during the welding step. The plasticised material is swept from the AS to RS during the FSW process to form the FSW joint. It is evident that the deformation of material at the AS and the RS is asymmetric, higher plastic strain occurs

in the AS than in the RS, which can be related to the positive impact of rotational and traverse speeds of the FSW tool, and the difference of material flows on both sides [72]. The results also reveal that the main deformation occurs near the top surface due to the larger contact area of the tool shoulder compared to the tool pin and the highest tool rotation speed. Furthermore, when the angular velocity of the tool increases from 800 rpm to 1100 rpm, the equivalent plastic strain increases with less difference between the AS and RS (more homogenous plastic deformation). This behaviour is confirmed by He et al. [12], and it is related to the fact that with an increase in the rotation of the tool per minute, the plastic deformation increases and hence improves the material flow.

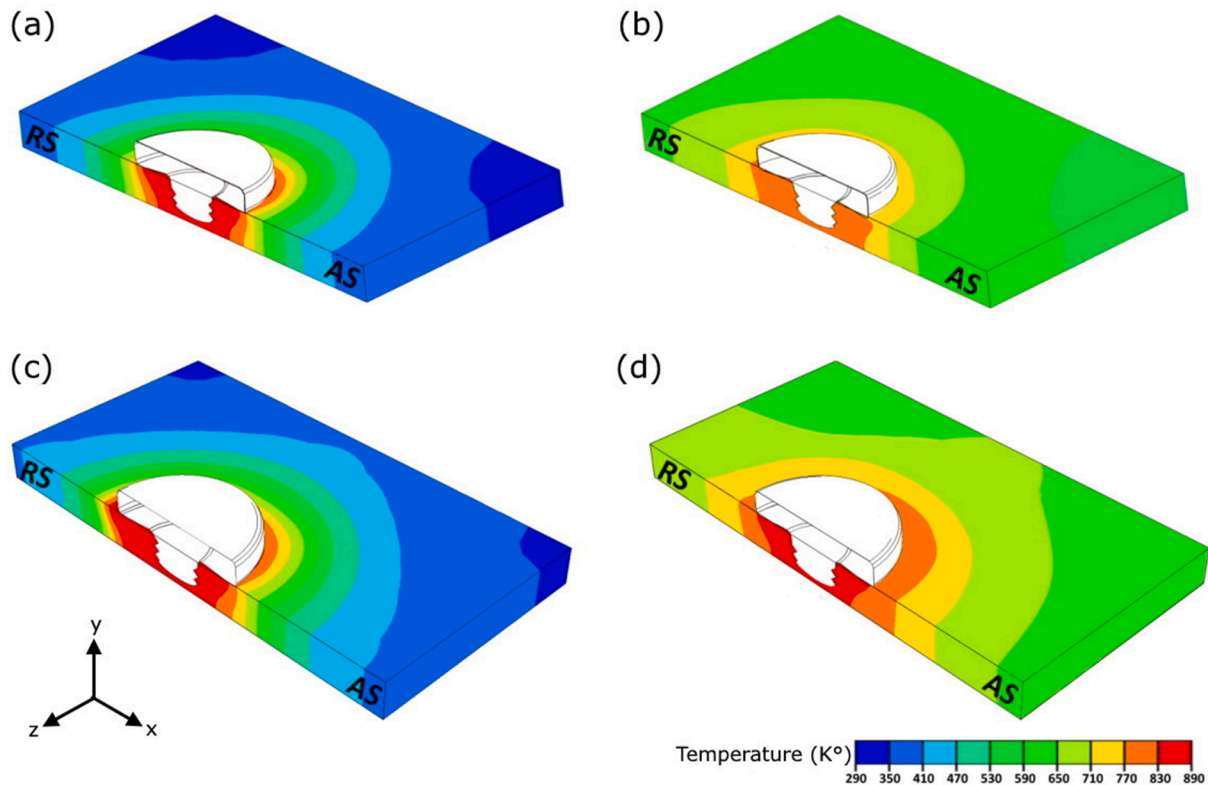


Fig. 8. Three-dimensional CEL simulation results show the temperature distribution in the cross-section of Weld I and Weld II - FSW joints at different steps. (a) Weld I - dwell step, (b) Weld I - welding step, (c) Weld II - dwell step, (d) Weld II - welding step. For all cases, the high temperature generated in the tool shoulder interface at the weld nugget area with a ‘V’ shape profile.

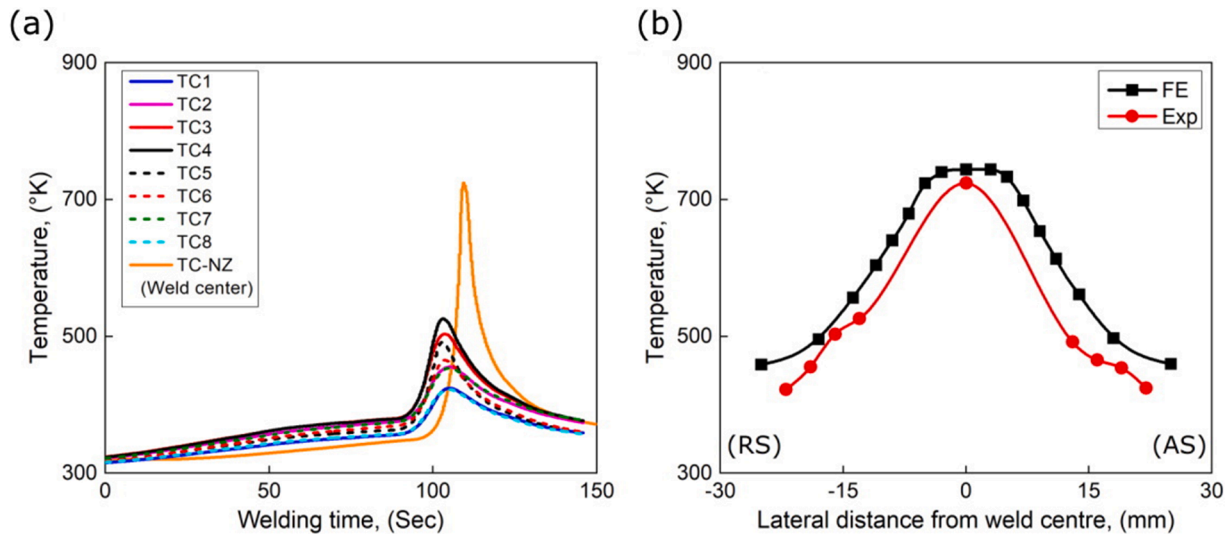


Fig. 9. Thermal history of Weld I - FSW joint (800 rpm-200 mm/min). (a) Experimentally measured temperature by thermocouples at different locations as a function of welding time; (TC1-TC4) on the retreating side, (TC5-TC8) on the advancing side, and (TC-NZ) in the middle of the nugget zone, (b) Comparison between the cross-weld temperature obtained from experimental measurements and FE model results. The higher temperature is 740° K generated in the centre of NZ.

This plastic strain behaviour, combined with thermal history (discussed in the previous section), significantly affects the formation of a sound welding joint.

Fig. 13 compares the simulated equivalent plastic strain distributions with the experimental macrostructure on the cross-section of Weld I and Weld II - FSW joints. Fig. 13(a) shows that low and inhomogeneous plastic deformation was generated during the welding process when using a lower tool rotation speed of 800 rpm (Weld I). This result in a

decrease in the flow of softened metal behind the welding tool, leading to insufficient mixing of metal during the welding phase and forming tunnel defects. As a result, the welding plate fails to be friction stir welded efficiently. The increasing rotational speed to 1100 rpm (Weld II) enhances plastic deformation and heat generation in the welding zone, which improves the flow of plasticised material and reduces the void size significantly, as shown in Fig. 13(b). Ajri et al. [56] have reported similar behaviour; the increase of tool rotation speed reduces and

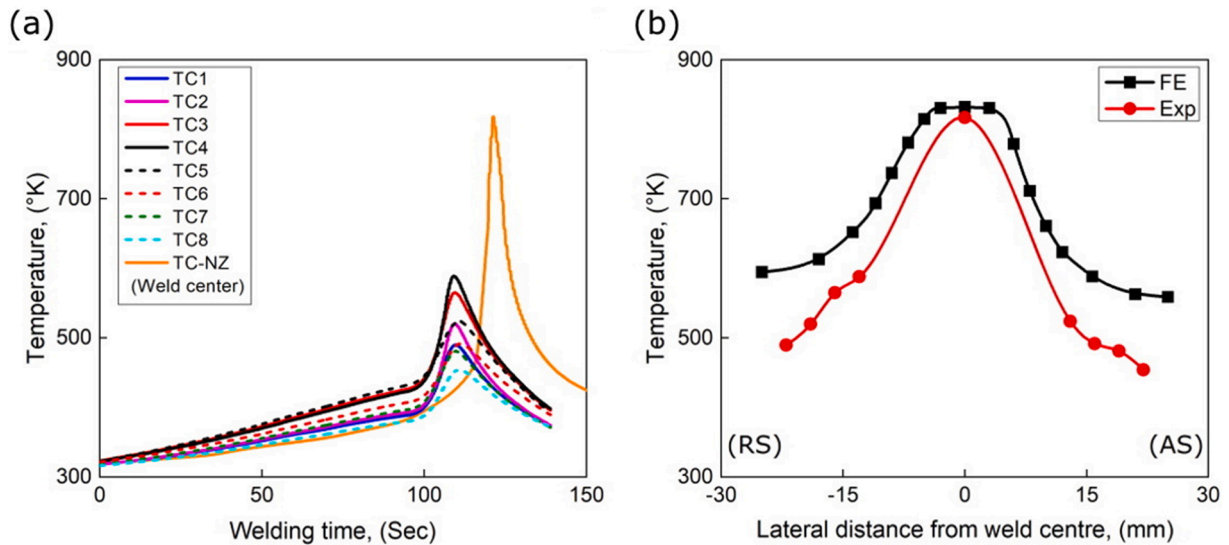


Fig. 10. Thermal history of Weld II - FSW joint (1100 rpm-200 mm/min). (a) Experimentally measured temperature by thermocouples at different locations as a function of welding time; (TC1-TC4) on the retreating side, (TC5-TC8) on the advancing side, and (TC-NZ) in the middle of the nugget zone, (b) Comparison between the cross-weld temperature obtained from experimental measurements and FE model results. The generated temperature in the NZ increases to around 850° K due to the higher rotation speed.

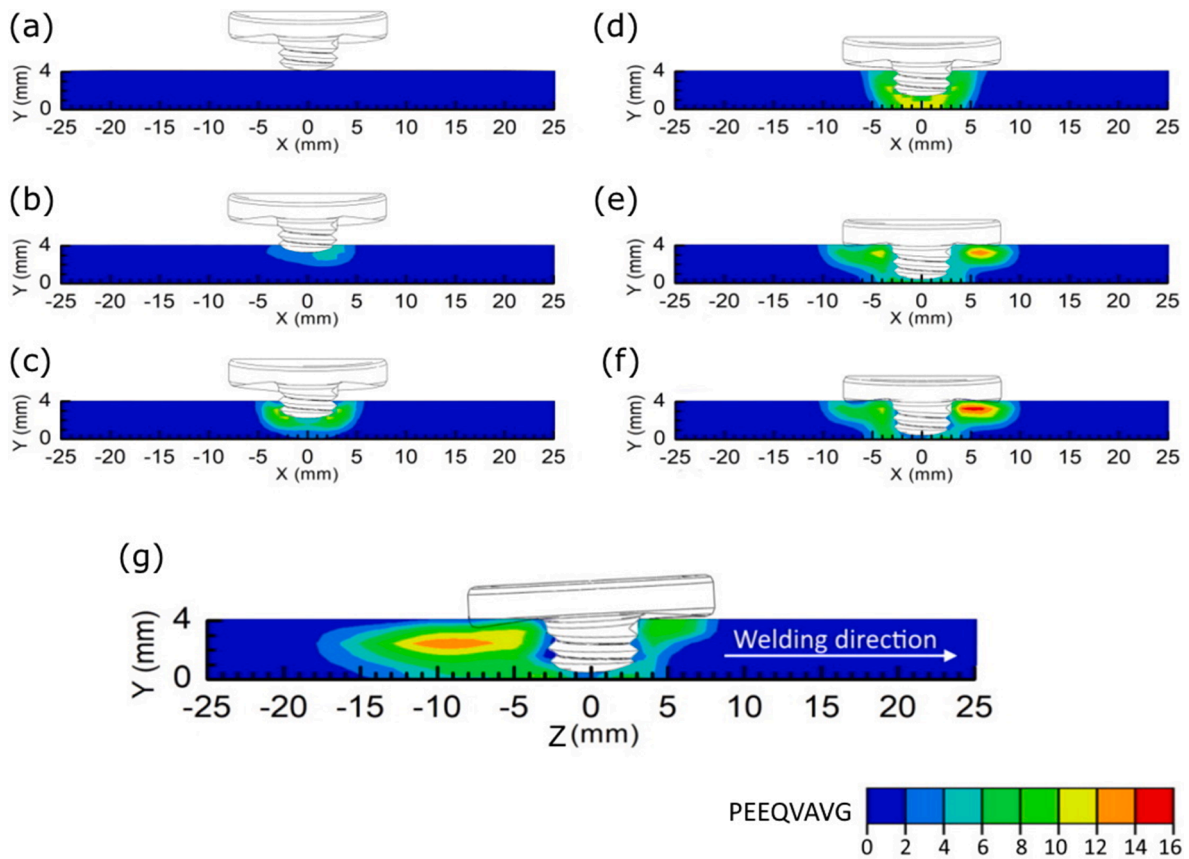


Fig. 11. Typical cross-weld equivalent plastic strain distributions in Weld I - FSW joint shows the deformation increases by increasing the tool plunge depth. (a-d) In the plunge step at plunge depths of 0, 0.9, 1.8 and 2.7 mm, respectively, (e) In the dwell step at a plunge depth of 3.5 mm, (f) In the welding step, (g) Longitudinal weld cross-section in the welding step shows the highest plastic strain area under the tool shoulder. (For a-f, AS on the right).

eliminates defect formation in FSW joints of Al 6061-T6. In addition, it is clear that the boundary of high plastic strain in the nugget zone of Weld II is larger than that in Weld I. This can be related to increasing the welding tool's stirring effect with the increased tool rotation speed.

4.3. Analysis and validation of residual stresses in FSW joint

Carone et al. [[73]] pointed out that the residual stresses introduced during the welding process are an essential consideration in welding

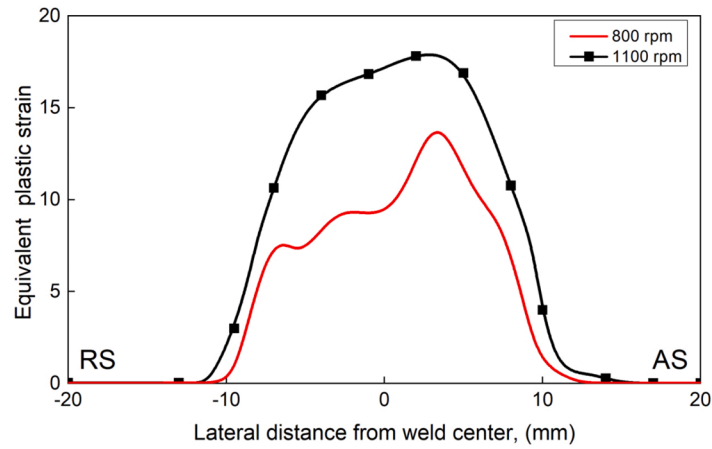


Fig. 12. Finite element results show tool rotation speed’s effect on equivalent plastic strain distribution through the cross-weld of FSW joints in the welding step for Weld I (800 rpm) and Weld II (1100 rpm) at a constant welding speed of 200 mm/min. Higher and more homogenous plastic deformation is obtained by increasing tool rotation speed to 1100 rpm.

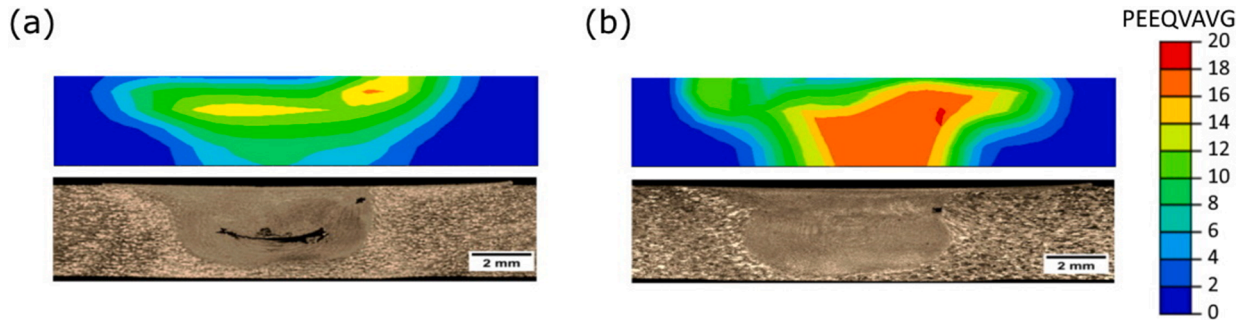


Fig. 13. The effect of tool rotation speed on the equivalent plastic strain and joint soundness. (a) Comparison of the equivalent plastic strain distributions with the experimental cross-weld macrostructure of Weld I - FSW joint. (b) Comparison of the equivalent plastic strain distributions with the experimental cross-weld macrostructure of Weld II - FSW joint. Increasing tool rotation speed to 1100 rpm leads to increased plastic deformation and reduced volumetric defects. (AS on the right).

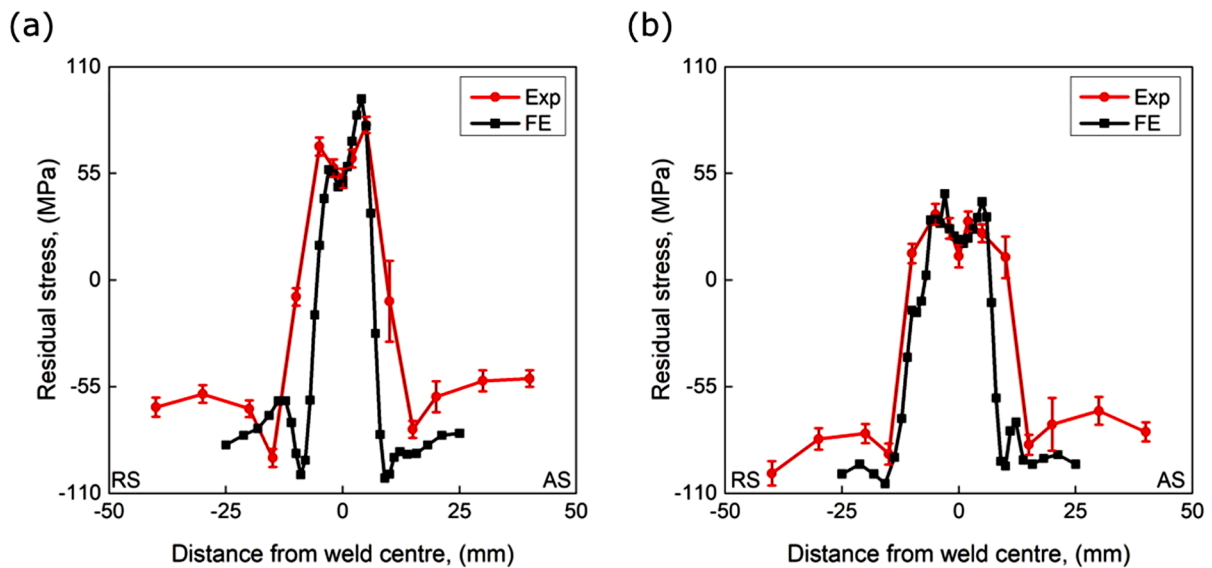


Fig. 14. Residual stress distribution in Weld II - FSW joint as a function of position relative to the weld centreline (cross-weld). (a) Comparison between experimental measurements and FE result of longitudinal residual stresses, and (b) Comparison between experimental measurements and FE result of transverse residual stresses. In both longitudinal and transverse directions, the residual stresses have an ‘M’ shaped profile, and the distribution of stresses in the longitudinal direction is asymmetric.

design because it directly affects the load capability of the welded structure. In addition, both Biallas [74] and Yadav et al. [75] confirmed that the induced residual stresses significantly affect the propagation rates of the near-threshold crack. The low inherent process-induced residual stresses are one of the main advantages of FSW over conventional welding processes because lower peak temperatures and hence reduced solidification-induced shrinkage can be achieved using FSW. However, Chen and Kovacevic [76] pointed out that the thermal and mechanical residual stresses developed in the FSW joints because of the expansion and contraction during the heating and cooling stages, as well as from the rotation and traverse movement of the FSW tool. The appearance of tensile stresses in the welding plate can cause crack initiation and increase crack growth rate leading to the increased possibility of failure and reduced service life. On the other hand, the compressive stress component can inhibit crack propagation [75].

Fig. 14 shows the typical distribution of longitudinal and transverse residual stresses as a function of distance from the weld line measured experimentally by neutron diffraction perpendicular to the cross-weld along the line AA (see Fig. 2), 2 mm below the top surface alongside with predicted results from the developed model for Weld II - FSW joint. The error bars were obtained based on the uncertainty for both the strain-free lattice parameter d_{hkl}^0 and the corresponding inter-planar distance d_{hkl}^i that arose from the Retvield method using GSAS. It can be seen that the residual stresses in LD and TD have an 'M' shaped profile. Double-peak tensile stresses are located at around ± 8 mm from the weld line just beyond the perimeter of the tool shoulder (near the BM / HAZ boundary). This profile is different from that often obtained in the fusion welding processes, where the peak residual tensile stress is along the centreline of the weld. Steuwer et al. [77] and He et al. [78] reported a similar stress profile in FSW joints of AA 6082 and AA 6005A, respectively. They attributed this behaviour to the non-uniform temperature distribution in the transverse section and the high shear force between the edge of the shoulder and the welded plate during the welding process. This behaviour is clearly noticed in the current work, as presented in Sections 4.1 and 4.2. Additionally, the drop in the tensile residual stress in the weld centre around the pin position was attributed by Feng et al. [79] and Sun et al. [80] to the dissolution of the strengthening precipitates and softening of the weld region caused by the high temperatures in this region, which would reduce the local yield stress and limit the material capacity to support the generated load.

Furthermore, it is evident from the figure that the tensile stress is higher in the longitudinal direction than in the transverse direction by around 30 MPa. The stress profile in the LD is slightly asymmetric concerning the welding centre; higher tensile stress is generated in the AS than in the RS. Similar behaviour was reported by Peel et al. [81] in friction stir weld of AA5083. This behaviour reflects the asymmetric nature of the FSW process and can be related to the relative motion between the rotating tool and the welded plate. He et al. [78] demonstrated that the relative speed on the AS is higher than that on the RS, producing additional tensile stress on the materials in the weld. To satisfy the equilibrium condition, the stress changes from tension to compression when moving further from the weld on either AS or RS and into the base metal. Although residual stresses are induced in the joint welded by FSW, it is still much lower than that can be obtained using fusion welding, which can approach the base metal yield strength [82]. Finally, the trends of residual stresses are correlated very well, and the CEL model captured the typical 'M' shaped profile with a double tensile region in the nugget zone below the shoulder of the FSW tool balanced by compression stress in the area far from the weld line.

5. Conclusions

A three-dimensional fully coupled thermo-mechanical FE model based on the Coupled Eulerian-Lagrangian (CEL) approach is employed to investigate the complex thermomechanical interaction mechanisms

in FSW. The model is used to qualitatively analyse the influence of tool rotation speeds on the quality of AA6082-T6 FSW joints by evaluating three crucial aspects, including thermal history, plastic deformation and material flow and residual stress. It is demonstrated that the model successfully simulates the whole steps of the FSW process (plunge, dwell, and welding) using the real complex geometry of the FSW tool (featureless concave profile shoulder and threaded cylindrical shape pin), which provides more realistic results and in-depth understanding to the complex interaction mechanisms in FSW processes. However, the issue of computational cost may still be the main concern.

The formation and evolution mechanisms of FSW joints are elucidated by analysing the numerical results of the CEL model and validation with the obtained experimental results. It is shown that, at a constant tool traverse speed, the tool rotation speeds influence the thermal history and plastic strain in the stirred volume during the welding process. With the increase of tool rotation speed, both generated temperature and plastic deformation in the stirring zone increase, which improves the welded metal's flowability and reduces the size of volumetric defects in the nugget zone, thus improving the quality of welded joints. Moreover, the thermal history analysis unveiled asymmetrical temperature distribution in the cross-weld section of the FSW joints. Higher heat is generated on the retreating side than on the advancing side. Also, the distribution of strain in the FSW joint is non-uniform; a higher strain is found on the top surface of the workpiece compared to the bottom surface, indicating the FSW process's nature.

The analysis of residual stress distribution in the FSW joint shows that the longitudinal residual stress is higher than the transverse one, and both of them are characterised by double-peak tensile stresses located at the advancing and retreating sides just beyond the perimeter of the tool shoulder, generating the unusual 'M' shaped profile, which is also reported in the other literature. The interpretation of this behaviour can be related to the non-uniform temperature distribution in the transverse section and the high shear force between the edge of the shoulder and the welded plate combined by strengthening precipitates dissolution in the weld region. The model also unveiled an asymmetric residual stress profile in the longitudinal direction where higher tensile stress is generated on the advanced side than on the retreated side.

The numerical and experimental results of thermal history, plastic deformation and residual stresses presented herein provide critical insight for analysing the bonding mechanisms and determining the weld quality of the FSW joints. Also, it demonstrates the feasibility and effectiveness of the CEL approach in modelling multi-physical problems such as FSW. The contribution of this work is evident as the resulting outcomes can be capitalised as guidelines to assess the weld quality under different welding parameters.

Declaration of Competing Interest

The authors declare that they have no known competing financial interests or personal relationships that could have appeared to influence the work reported in this paper.

Data Availability

The raw/processed data required to reproduce these findings cannot be shared at this time due to technical or time limitations.

Acknowledgments

The first author would like to thank the financial support of the Ministry of Higher Education and Scientific Research (MOHESR), Iraq, through scholarship no. 5032. The authors thank the Science and Technology Facilities Council (STFC) for providing access to neutron beamtime at ISIS, ENGIN-X facilities, and Dr Joe Kelleher for technical assistance. The authors also thank TWI Ltd Technology Centre

(Yorkshire) for providing access to the FSW machine and Dr Xingguo Wei for technical assistance.

Appendix

Governing equations

In the current work, the FSW tool was modelled as a Lagrangian body, and the workpiece was modelled under the Eulerian framework. In the Lagrangian description, the mass, momentum and energy conservation equations are written using material time derivatives, as given by Eqs. (10)–(12), respectively.

$$\frac{D\rho}{Dt} + \rho \nabla \cdot \mathbf{v} = 0 \quad (10)$$

$$\rho \frac{D\mathbf{v}}{Dt} = \nabla \cdot \boldsymbol{\sigma} + \rho \mathbf{b} \quad (11)$$

$$\frac{DE}{Dt} = \nabla \cdot (\boldsymbol{\sigma} \cdot \mathbf{v}) + \rho \mathbf{b} \cdot \mathbf{v} \Rightarrow \left\{ E = \frac{1}{2} \rho \mathbf{v} \cdot \mathbf{v} + e \right\} \Rightarrow \frac{De}{Dt} = \boldsymbol{\sigma} : \mathbf{D} \quad (12)$$

Where ρ , \mathbf{v} , $\boldsymbol{\sigma}$, \mathbf{b} , E , e and \mathbf{D} are the density, material velocity, Cauchy stress, body forces, total energy per unit volume, internal energy, and velocity strain, respectively. In Eulerian analyses, the conservation equations are written using spatial time derivatives. Material and spatial time derivatives can be correlated with each other based on Eq. (13) [83]. Therefore, for the FSW problem, this equation is used to transform the conservation equations of the Lagrangian analysis (material time derivative Eqs. (10)–(12)) to Eulerian analysis (spatial time derivative), as given in Eqs. (14)–(16), respectively.

$$\frac{D\Phi}{Dt} = \frac{\partial \Phi}{\partial t} + \mathbf{v} \cdot (\nabla \Phi) \quad (13)$$

$$\frac{\partial \rho}{\partial t} + \mathbf{v} \cdot (\nabla \rho) + \rho \nabla \cdot \mathbf{v} = 0 \quad (14)$$

$$\frac{\partial \mathbf{v}}{\partial t} + \mathbf{v} \cdot (\nabla \cdot \mathbf{v}) = \frac{1}{\rho} (\nabla \cdot \boldsymbol{\sigma}) + \mathbf{b} \quad (15)$$

$$\frac{\partial e}{\partial t} + \mathbf{v} \cdot (\nabla e) = \boldsymbol{\sigma} : \mathbf{D} \quad (16)$$

Where Φ , $\frac{D\Phi}{Dt}$, and $\frac{\partial \Phi}{\partial t}$ represent the arbitrary solution variable, material time derivatives, and spatial time derivatives, respectively. Furthermore, these Eulerian equations can be written in conservative forms, as given in Eqs. (17)–(19).

$$\frac{\partial \rho}{\partial t} + \nabla \cdot (\rho \mathbf{v}) = 0 \quad (17)$$

$$\frac{\partial \rho \mathbf{v}}{\partial t} + \nabla \cdot (\rho \mathbf{v} \otimes \mathbf{v}) = \nabla \cdot \boldsymbol{\sigma} + \rho \mathbf{b} \quad (18)$$

$$\frac{\partial e}{\partial t} + \nabla \cdot (e \mathbf{v}) = \boldsymbol{\sigma} : \mathbf{D} \quad (19)$$

In order to solve the problem, the Eulerian governing Eqs. (17)–(19) are rewritten to the general form, as shown in Eq. (20).

$$\frac{\partial \Phi}{\partial t} + \nabla \cdot \boldsymbol{\varphi} = \mathbf{S} \quad (20)$$

Where $\boldsymbol{\varphi}$ and \mathbf{S} are the flux function and source term, respectively, this equation can be divided into two equations Eqs. (21) and ((22)) using the operator splitting method to be solved sequentially in the CEL approach.

$$\frac{\partial \Phi}{\partial t} = \mathbf{S} \quad (21)$$

$$\frac{\partial \Phi}{\partial t} + \nabla \cdot \boldsymbol{\varphi} = 0 \quad (22)$$

In fully coupled thermal-stress analysis, the heat transfer equations are integrated using the explicit forward-difference time integration rule in the current time step, as presented in Eq. (23)

$$T_{i+1} = T_i + \Delta t_{i+1} \dot{T}_i \quad (23)$$

Where T and i represent the temperature and increment number in an explicit dynamic step, respectively. The current temperatures are obtained using

known values of \dot{T}_i from the previous increment. The temperature rate vector, \dot{T}_i , is calculated at the end of the time increment i , as presented in Eq. (24)

$$\dot{T}_i = (C^{NJ})^{-1} (P'_{(i)} - F'_{(i)}) \quad (24)$$

Where C^{NJ} , P^J and F^J are the lumped capacitance matrix, applied nodal source vector, and internal flux vector, respectively.

The mechanical solution response is obtained using the explicit central-difference integration rule with a lumped mass matrix in the current time step as described in Eqs. (25) and (26).

$$\dot{u}_{i+1/2} = \dot{u}_{i-1/2} + \frac{\Delta t_{i+1} + \Delta t_i}{2} \ddot{u}_i \quad (25)$$

$$u_{i+1} = u_i + \Delta t_{i+1} \dot{u}_{i+1/2} \quad (26)$$

The acceleration vector at the end of the time increments i is computed by Eq. (27)

$$\ddot{u}_i = M^{-1} (L_i - I_i) \quad (27)$$

Where M , L and I represent the diagonal mass matrix, applied load vector, and internal force vector, respectively.

An incompressible rigid-perfect Mises plastic constitutive model was used to measure the stresses with the following equations.

$$\sigma_y = \sqrt{\frac{3}{2}} S : S \quad (28)$$

$$\dot{\bar{\epsilon}} = \sqrt{\frac{2}{3}} \epsilon : \epsilon \quad (29)$$

$$\epsilon = \frac{\partial \sigma_y}{\partial S} = \frac{3\dot{\bar{\epsilon}}}{2\sigma_y} = \frac{S}{2\vartheta} \quad (30)$$

Where σ_y , S , $\dot{\bar{\epsilon}}$, ϵ and ϑ are von Mises effective yield stress, deviatoric Cauchy stress tensor, conjugate effective strain rate, deformation rate, and viscosity, respectively.

References

- Heidarzadeh A, Mironov S, Kaibyshev R, Çam G, Simar A, Gerlich A, Khodabakhshi F, Mostafaei A, Field DP, Robson JD. Friction stir welding/processing of metals and alloys: a comprehensive review on microstructural evolution. *Prog Mater Sci* 2021;117:100752.
- Meng X, Huang Y, Cao J, Shen J, dos Santos JF. Recent progress on control strategies for inherent issues in friction stir welding. *Prog Mater Sci* 2021;115:100706.
- Verma S, Kumar V, Kumar R, Sidhu RS. Exploring the application domain of friction stir welding in aluminum and other alloys. *Mater Today Proc* 2022;50:1032–42.
- Malik V, Kailas SV. Plasticine modeling of material mixing in friction stir welding. *J Mater Process Technol* 2018;258:80–8.
- Gite RA, Loharkar PK, Shimpi R. Friction stir welding parameters and application: a review. *Mater Today Proc* 2019;19:361–5.
- Salih OS, Ou H, Sun W, McCartney D. A review of friction stir welding of aluminium matrix composites. *Mater Des* 2015;86:61–71.
- Imam M, Biswas K, Racherla V. On use of weld zone temperatures for online monitoring of weld quality in friction stir welding of naturally aged aluminium alloys. *Mater Des* 2013;52:730–9.
- Assidi M, Fourment L, Guerdoux S, Nelson T. Friction model for friction stir welding process simulation: calibrations from welding experiments. *Int J Mach Tools Manuf* 2010;50:143–55.
- Myung D, Noh W, Kim JH, Kong J, Hong ST, Lee MG. Probing the mechanism of friction stir welding with ALE based finite element simulations and its application to strength prediction of welded aluminum. *Met Mater Int* 2021;27:650–66.
- Hasan A, Bennett C, Shipway P. A numerical comparison of the flow behaviour in Friction Stir Welding (FSW) using unworn and worn tool geometries. *Mater Des* 2015;87:1037–46.
- Jedrasiak P, Shercliff H. Small strain finite element modelling of friction stir spot welding of Al and Mg alloys. *J Mater Process Technol* 2019;263:207–22.
- He X, Gu F, Ball A. A review of numerical analysis of friction stir welding. *Prog Mater Sci* 2014;65:1–66.
- Mijajlović M, Milčić D, Milčić M. Numerical simulation of friction stir welding. *Therm Sci* 2014;18:967–78.
- Chen G, Zhang S, Zhu Y, Yang C, Shi Q. Thermo-mechanical analysis of friction stir welding: A review on recent advances. *Acta Metall Sin* 2020;33:3–12 (English Letters).
- Seidel T, Reynolds AP. Two-dimensional friction stir welding process model based on fluid mechanics. *Sci Technol Weld Join* 2003;8:175–83.
- Colegrove P, Shercliff H. Two-dimensional CFD modelling of flow round profiled FSW tooling. *Sci Technol Weld Join* 2004;9:483–92.
- Colegrove PA, Shercliff H. Development of Trivex friction stir welding tool Part 2—three-dimensional flow modelling. *Sci Technol Weld Join* 2004;9:352–61.
- Colegrove PA, Shercliff HR. 3-Dimensional CFD modelling of flow round a threaded friction stir welding tool profile. *J Mater Process Technol* 2005;169:320–7.
- Zhang S, Chen G, Liu Q, Li H, Zhang G, Wang G, Shi Q. Numerical analysis and analytical modeling of the spatial distribution of heat flux during friction stir welding. *J Manuf Process* 2018;33:245–55.
- Hasan A. CFD modelling of friction stir welding (FSW) process of AZ31 magnesium alloy using volume of fluid method. *J Mater Res Technol* 2019;8:1819–27.
- Zhai M, Wu C, Su H. Influence of tool tilt angle on heat transfer and material flow in friction stir welding. *J Manuf Process* 2020;59:98–112.
- Shi L, Wu C, Liu X. Modeling the effects of ultrasonic vibration on friction stir welding. *J Mater Process Technol* 2015;222:91–102.
- Shi L, Wu C, Fu L. Effects of tool shoulder size on the thermal process and material flow behaviors in ultrasonic vibration enhanced friction stir welding. *J Manuf Process* 2020;53:69–83.
- Zhao W, Wu C, Shi L. Acoustic induced antifriction and its effect on thermo-mechanical behavior in ultrasonic assisted friction stir welding. *Int J Mech Sci* 2021;190:106039.
- Kaid M, Zemri M, Brahami A, Zahaf S. Effect of friction stir welding (FSW) parameters on the peak temperature and the residual stresses of aluminum alloy 6061-T6: numerical modelisation. *Int J Interact Des Manuf* 2019;13:797–807.
- Wu W, Zhang AM, Liu M. A cell-centered indirect Arbitrary-Lagrangian-Eulerian discontinuous Galerkin scheme on moving unstructured triangular meshes with topological adaptability. *J Comput Phys* 2021;438:110368.
- Ansari MA, Behnagh RA, Salvadori A. Numerical analysis of high-speed water jet spot welding using the arbitrary Lagrangian-Eulerian (ALE) method. *Int J Adv Manuf Technol* 2021;112:491–504.
- Schmidt H, Hattel J. A local model for the thermomechanical conditions in friction stir welding. *Modell Simul Mater Sci Eng* 2005;13:77–93.
- Deng X, Xu S. Two-dimensional finite element simulation of material flow in the friction stir welding process. *J Manuf Process* 2004;6:125–33.
- Zhang H, Zhang Z, Chen J. The finite element simulation of the friction stir welding process. *Mater Sci Eng A* 2005;403:340–8.
- Zhang H, Zhang Z, Chen J. 3D modeling of material flow in friction stir welding under different process parameters. *J Mater Process Technol* 2007;183:62–70.
- Zhang Z. Comparison of two contact models in the simulation of friction stir welding process. *J Mater Sci* 2008;43:5867–77.

- [33] Dialami N, Chiumenti M, Cervera M, Segatori A, Osikowicz W. Enhanced friction model for Friction Stir Welding (FSW) analysis: simulation and experimental validation. *Int J Mech Sci* 2017;133:555–67.
- [34] Dialami N, Cervera M, Chiumenti M, Segatori A. Prediction of joint line remnant defect in friction stir welding. *Int J Mech Sci* 2019;151:61–9.
- [35] Dialami N, Cervera M, Chiumenti M. Defect formation and material flow in friction stir welding. *Eur J Mech A Solids* 2020;80:103912.
- [36] Andrade D, Leitão C, Dialami N, Chiumenti M, Rodrigues D. Modelling torque and temperature in friction stir welding of aluminium alloys. *Int J Mech Sci* 2020;182:105725.
- [37] Andrade D, Leitão C, Dialami N, Chiumenti M, Rodrigues D. Analysis of contact conditions and its influence on strain rate and temperature in friction stir welding. *Int J Mech Sci* 2021;191:106095.
- [38] Tongne A, Desrayaud C, Jahazi M, Feulvarch E. On material flow in friction stir welded Al alloys. *J Mater Process Technol* 2017;239:284–96.
- [39] Benson DJ. A mixture theory for contact in multi-material Eulerian formulations. *Comput Meth Appl Mech Eng* 1997;140:59–86.
- [40] Al-Badour F, Merah N, Shuaib A, Bazoune A. Coupled Eulerian Lagrangian finite element modeling of friction stir welding processes. *J Mater Process Technol* 2013;213:1433–9.
- [41] Chauhan P, Jain R, Pal SK, Singh SB. Modeling of defects in friction stir welding using coupled Eulerian and Lagrangian method. *J Manuf Process* 2018;34:158–66.
- [42] Su Y, Li W, Liu X, Gao F, Yu Y, Vairis A. Strengthening mechanism of friction stir welded alpha titanium alloy specially designed T-joints. *J Manuf Process* 2020;55:1–12.
- [43] Akbari M, Asadi P, Behnagh RA. Modeling of material flow in dissimilar friction stir lap welding of aluminum and brass using Coupled Eulerian and Lagrangian method. *Int J Adv Manuf Technol* 2021;113:721–34.
- [44] Wang X, Gao Y, Liu X, McDonnell M, Feng Z. Tool-workpiece stick-slip conditions and their effects on torque and heat generation rate in the friction stir welding. *Acta Mater* 2021;213:116969.
- [45] Salih OS, Neate N, Ou H, Sun W. Influence of process parameters on the microstructural evolution and mechanical characterisations of friction stir welded Al-Mg-Si alloy. *J Mater Process Technol* 2020;275:116366.
- [46] Santisteban J, Daymond M, James J, Edwards L. ENGIN-X: a third-generation neutron strain scanner. *J Appl Crystallogr* 2006;39:812–25.
- [47] Torić N, Brnić J, Boko I, Brčić M, Burgess IW, Uzelac I. Experimental analysis of the behaviour of aluminium alloy EN 6082AW T6 at high temperature. *Metals* 2017;7:126.
- [48] Payandeh M, Sjölander E, Jarfors AE, Wessen M. Mechanical and thermal properties of rheocast telecom component using low silicon aluminium alloy in as-cast and heat-treated conditions. *Light metals* 2015. Springer; 2015. p. 209–14.
- [49] Wilson A. The thermal expansion of aluminium from 0 to 650 C. *Proc Phys Soc* 1941;53:235.
- [50] Jaspers S, Dautzenberg J. Material behaviour in conditions similar to metal cutting: flow stress in the primary shear zone. *J Mater Process Technol* 2002;122:322–30.
- [51] Malik V, Saxena K. Understanding tool–workpiece interfacial friction in friction stir welding/processing and its effect on weld formation. *Adv Mater Process Technol* 2022:1–17.
- [52] Nandan R, DebRoy T, Bhadeshia H. Recent advances in friction-stir welding—process, weldment structure and properties. *Prog Mater Sci* 2008;53:980–1023.
- [53] Asadi P, Mirzaei M, Akbari M. Modeling of pin shape effects in bobbin tool FSW. *Int J Lightweight Mater Manuf* 2022;5:162–77.
- [54] Wang X, Gao Y, McDonnell M, Feng Z. Determination of the friction stir welding window from the solid-state-bonding mechanics under severe thermomechanical conditions. *Materialia* 2022;21:101350.
- [55] Wen Q, Li W, Wang W, Wang F, Gao Y, Patel V. Experimental and numerical investigations of bonding interface behavior in stationary shoulder friction stir lap welding. *J Mater Sci Technol* 2019;35:192–200.
- [56] Ajri A, Rohatgi N, Shin YC. Analysis of defect formation mechanisms and their effects on weld strength during friction stir welding of Al 6061-T6 via experiments and finite element modeling. *Int J Adv Manuf Technol* 2020;107:4621–35.
- [57] Rathinasuriyan C, Muniyandhu S, Mystica A, Kumar VS. Investigation of heat generation during submerged friction stir welding on 6061-T6 aluminum alloy. *Mater Today Proc* 2021;46:8320–4.
- [58] Kumar K, Kalyan C, Kailas SV, Srivatsan TS. An investigation of friction during friction stir welding of metallic materials. *Mater Manuf Process* 2009;24:438–45.
- [59] Zhang Z, Zhang H. Numerical studies on controlling of process parameters in friction stir welding. *J Mater Process Technol* 2009;209:241–70.
- [60] Hassanamraji N, Eivani AR, Aboutalebi MR. Finite element simulation of deformation and heat transfer during friction stir processing of as-cast AZ91 magnesium alloy. *J Mater Res Technol* 2021;14:2998–3017.
- [61] Jain R, Pal SK, Singh SB. Finite element simulation of pin shape influence on material flow, forces in friction stir welding. *Int J Adv Manuf Technol* 2018;94:1781–97.
- [62] Ragab M, Liu H, Yang GJ, Ahmed MM. Friction stir welding of 1Cr11Ni2W2MoV martensitic stainless steel: Numerical simulation based on coupled Eulerian Lagrangian approach supported with experimental work. *Appl Sci* 2021;11:3049.
- [63] Saha R, Biswas P. Temperature and stress evaluation during friction stir welding of inconel 718 alloy using finite element numerical simulation. *J Mater Eng Perform* 2022;31:2002–11.
- [64] Ghiasvand A, Suksatan W, Tomków J, Rogalski G, Derazkola HA. Investigation of the effects of tool positioning factors on peak temperature in dissimilar friction stir welding of AA6061-T6 and AA7075-T6 aluminum alloys. *Materials* 2022;15:702.
- [65] Nandan R, Roy G, Lienert T, DebRoy T. Numerical modelling of 3D plastic flow and heat transfer during friction stir welding of stainless steel. *Sci Technol Weld Join* 2006;11:526–37.
- [66] Rui-Dong F, Zeng-Qiang S, Rui-Cheng S, Ying L, Hui-jie L, Lei L. Improvement of weld temperature distribution and mechanical properties of 7050 aluminum alloy butt joints by submerged friction stir welding. *Mater Des* 2011;32:4825–31.
- [67] Abulosoro OP, Akinlabi ET, Kailas SV. Tool rotational speed impact on temperature variations, mechanical properties and microstructure of friction stir welding of dissimilar high-strength aluminium alloys. *J Braz Soc Mech Sci Eng* 2020;42:176.
- [68] Commin L, Dumont M, Masse JE, Barrallier L. Friction stir welding of AZ31 magnesium alloy rolled sheets: Influence of processing parameters. *Acta Mater* 2009;57:326–34.
- [69] Abnar B, Kazeminezhad M, Kokabi A. Effects of heat input in friction stir welding on microstructure and mechanical properties of AA3003-H18 plates. *Trans Nonferrous Met Soc China* 2015;25:2147–55.
- [70] Ke L, Xing L, Indacochea J. Material flow patterns and cavity model in friction-stir welding of aluminum alloys. *Metall Mater Trans B* 2004;35:153–60.
- [71] Neto DM, Neto P. Numerical modeling of friction stir welding process: a literature review. *Int J Adv Manuf Technol* 2013;65:115–26.
- [72] Jain R, Pal SK, Singh SB. Finite element simulation of temperature and strain distribution during friction stir welding of AA2024 aluminum alloy. *J Inst Eng India Ser C* 2017;98:37–43.
- [73] Carone S, Moramarco V, Pappalettera G, Barbieri G, Casavola C. Residual stress measurement on Titanium Grade 5 and Inconel 625 thin dissimilar welded joints by contour method. *J Mater Sci* 2022;57:671–86.
- [74] Biallas G. Effect of welding residual stresses on fatigue crack growth thresholds. *Int J Fatigue* 2013;50:10–7.
- [75] Yadav VK, Gaur V, Singh I. Combined effect of residual and mean stresses on fatigue behavior of welded aluminum 2024 alloy. *Int J Fatigue* 2022;155:106565.
- [76] Chen C, Kovacevic R. Parametric finite element analysis of stress evolution during friction stir welding. *Proc Inst Mech Eng Part B J Eng Manuf* 2006;220:1359–71.
- [77] Steuwer A, Peel M, Withers P. Dissimilar friction stir welds in AA5083-AA6082: the effect of process parameters on residual stress. *Mater Sci Eng A* 2006;441:187–96.
- [78] He W, Liu J, Hu W, Wang G, Chen W. Controlling residual stress and distortion of friction stir welding joint by external stationary shoulder. *High Temp Mater Process* 2019;38:662–71.
- [79] Feng Z, Wang XL, David SA, Sklad PS. Modelling of residual stresses and property distributions in friction stir welds of aluminium alloy 6061-T6. *Sci Technol Weld Join* 2007;12:348–56.
- [80] Sun T, Roy M, Strong D, Withers PJ, Prangnell PB. Comparison of residual stress distributions in conventional and stationary shoulder high-strength aluminum alloy friction stir welds. *J Mater Process Technol* 2017;242:92–100.
- [81] Peel M, Steuwer A, Preuss M, Withers P. Microstructure, mechanical properties and residual stresses as a function of welding speed in aluminium AA5083 friction stir welds. *Acta Mater* 2003;51:4791–801.
- [82] Gao S, Geng S, Jiang P, Han C, Ren L. Numerical study on the effect of residual stress on mechanical properties of laser welds of aluminum alloy 2024. *Opt Laser Technol* 2022;146:107580.
- [83] Benson DJ, Okazawa S. Contact in a multi-material Eulerian finite element formulation. *Comput Meth Appl Mech Eng* 2004;193:4277–98.